Available online at www.sciencedirect.com
SCIENCE DIRECT®
C. R. Physique 4 (2003) 1133–1154
COMPTES RENDUS PHYSIQUE

IR vision: from chip to image/Vision IR : du composant à l'image

Infrared photodetection with semiconductor self-assembled quantum dots

Philippe Boucaud *, Sébastien Sauvage

Institut d'électronique fondamentale, unité mixte de recherche CNRS 8622, bâtiment 220, Université Paris-Sud, 91405 Orsay, France

Presented by Guy Laval

Abstract

Semiconductor self-assembled quantum dots are potential candidates to develop a new class of midinfrared quantum photodetectors and focal plane arrays. In this article, we present the specific midinfrared properties of InAs/GaAs quantum dots associated with the intersublevel transitions. The electronic structure, which accounts for the strain field in the islands, is obtained within the framework of a three-dimensional 8 band **k**.**p** formalism. The midinfrared intersublevel absorption in *n*-doped quantum dots is described. We show that the carrier dynamics can be understood in terms of polarons which result from the strong coupling regime for the electron–phonon interaction in the dots. The principle of operation of vertical and lateral quantum dot infrared photodetectors is described and discussed by comparison with quantum well infrared photodetectors. We review the performances of different type of detectors developed to date and finally give some orientation to realize high performance quantum dot infrared photodetectors. ***To cite this article: P. Boucaud, S. Sauvage, C. R. Physique 4 (2003).***
© 2003 Published by Elsevier SAS on behalf of Académie des sciences.

Résumé

Photodétection infrarouge avec les boîtes quantiques semi-conductrices auto-assemblées. Les boîtes quantiques semi-conductrices auto-assemblées sont des candidates pour le développement d'une nouvelle classe de photodétecteurs quantiques et de matrices fonctionnant dans le moyen infrarouge. Dans cet article, nous décrivons les propriétés des transitions intersousniveaux des boîtes quantiques InAs/GaAs. La structure électronique qui tient compte du champ de contrainte dans les boîtes est obtenue dans un formalisme **k**.**p** à 8 bandes en tenant compte du confinement tridimensionnel. L'absorption intersousniveaux dans le moyen infrarouge de boîtes quantiques dopées *n* est décrite. Nous montrons que la dynamique des porteurs peut être comprise dans le cadre d'une théorie de polarons qui résulte du régime de couplage fort pour l'interaction électron–phonon dans les boîtes. Le principe de fonctionnement de photodétecteurs moyen infrarouge à boîtes quantiques verticaux et latéraux est décrit et discuté par référence à celui des photodétecteurs à puits quantiques. Les performances de différents types de détecteurs développés à ce jour sont présentées et nous donnons des directions pour la réalisation de photodétecteurs moyen infrarouge à boîtes quantiques performants. ***Pour citer cet article : P. Boucaud, S. Sauvage, C. R. Physique 4 (2003).***
© 2003 Published by Elsevier SAS on behalf of Académie des sciences.

1. Introduction

Photon detectors operating in the 3–5 μm or 8–12 μm transparency windows of the atmosphere are very important devices for high resolution imaging, military targeting and tracking, and environmental monitoring. A new class of infrared photodetectors taking advantage of the quantum confinement obtained in semiconductor heterostructures has emerged recently. These novel

* Corresponding author.
E-mail addresses: philippe.boucaud@ief.u-psud.fr (P. Boucaud), sebastien.sauvage@ief.u-psud.fr (S. Sauvage).

1631-0705/$ – see front matter © 2003 Published by Elsevier SAS on behalf of Académie des sciences.
doi:10.1016/j.crhy.2003.10.020

photodetectors correspond to the so-called quantum well infrared photodetectors (QWIPs) where the photoexcitation of the carriers relies on intersubband absorption in semiconductors quantum wells [1,2]. Taking advantage of the maturity of the III–V technology, high-sensitivity focal plane arrays operating in the midinfrared spectral range have been successfully developed. This successful development was the consequence of the so-called band gap and wave function engineering which is allowed by tailoring the composition and the thicknesses of quantum wells. In the case of semiconductor quantum wells the quantization occurs along one space direction and the bound states correspond to subbands (at the origin of the term intersubband transition) where the carriers can freely move in the layer plane. The degree of quantization can be increased in semiconductor heterostructures, leading to semiconductor quantum wires or semiconductor quantum dots (QDs) where the confinement occurs along the three space-directions.

In semiconductor quantum dots, the three-dimensional (3D) confinement leads to very specific features like a delta-like density of states. This δ-like density of states which is similar to that observed in atoms is expected to lead to strong modifications of the optoelectronic properties, like a slowing of the relaxation processes [3]. Optical transitions can be observed between the three-dimensionally confined states of the quantum dots either between the conduction states or the valence states. These transitions are usually referred to as *intersublevel* or *intraband* transitions. It is clear that there is a strong analogy between the intersublevel transitions in quantum dots and the intersubband transitions in quantum wells. As a consequence, optical processes associated with intersubband transitions like absorption, emission, or nonlinearities which have been successfully observed in quantum wells are expected to be observed in quantum dots. Although the analogy between intersublevel and intersubband transitions is certainly useful, one has to keep in mind that the three-dimensional potential confinement can lead to very specific features that are not observed in quantum wells. The study of quantum dot intersublevel transitions and its application to photodetection represents therefore a specific domain, distinct from intersubband transitions in quantum wells.

Semiconductor quantum dots can be grown or engineered by many different techniques. Depending on the thicknesses associated with the potential confinement, the energy of the intersublevel transitions can exhibit resonances varying from the midinfrared to the far infrared spectral range. A first approach to realize quantum dots consists of lateral or post-growth structuring of two-dimensional layers. The lateral confinement is either achieved using standard photolithography techniques or by depleting the gas carrier with electrostatically defined gates [4]. These techniques have been successfully applied to study the transport properties of quantum dots [5]. First observations of intersublevel transitions in the far infrared have been reported in the early 1990s, either in InSb-based electrostatically defined quantum dots [6] or in structured two-dimensional electron gas [7]. In the latter cases, the intersublevel transitions were resonant in the far infrared because of the large lateral sizes of the quantum dots.

One of the most popular ways to realize quantum dots is to rely on a spontaneous formation process. This can be achieved in the so-called Stranski–Krastanow growth mode [8] that occurs during the epitaxial growth between lattice-mismatched semiconductors. The quantum dot formation is driven by the strain accumulated in the epitaxial layer. Above a given critical thickness of the wetting layer (WL), islands with scales ranging in the nanometer range are spontaneously formed. This growth mode can be successfully obtained by different growth techniques, including molecular beam epitaxy, chemical vapor deposition, or metal-organic chemical vapor deposition. To date, the most studied type of self-assembled quantum dots is the InAs/GaAs system, which can be considered as a model system [9]. However, since the key parameter which governs the growth is the lattice-mismatch between the semiconductors (7% in the case of InAs on GaAs), self-assembled quantum dots can be easily obtained with other materials like germanium and silicon [10]. The interest for self-assembled quantum dots relies not only on the easy formation process but also on their potential applications due to their compatibility and their possible integration with standard III–V and IV–IV electronics.

Depending on the growth conditions, self-assembled quantum dots with different mean sizes, shapes and compositions can be obtained. In the case of the InAs/GaAs heterosystem, self-assembled quantum dots with various shapes have been reported in the literature, including lens-shaped quantum dots [11] square-based pyramids [12] or elongated pyramids [13]. Different aspect ratios, defined as the height divided by the base or diameter, have also been reported. The lens-shaped quantum dots are usually rather flat, with an aspect ratio of the order of $1:10$, with typical dimension of 2.5 nm height and 25 nm diameter [11]. The pyramids exhibit facets with higher index planes and higher aspect ratios $(1:2)$. We emphasize that the composition, the strain-relaxation, the interdiffusion and the segregation are strongly dependent on the growth parameters, like the temperature, the ratio between the III–V elements fluxes, the capping procedure etc. It is therefore very difficult to compare quantitatively the results which have been reported in the literature so far. The electronic spectrum of the dots is dependent on all these parameters, and in turn is expected to vary from one system to another. However, as will be shown below, the general properties (i.e., absorption, carrier dynamics) associated with intersublevel transitions can be understood without getting into the details of the composition and geometry.

One drawback of the self-assembled quantum dots as compared to lithography-defined quantum dots is their size distribution, which can put a limitation for device application. The size dispersion, which is inherent to the Stranski–Krastanow growth mode formation, is generally of the order of a few percent around the mean size. The mean size can evidently be varied during the growth process, which opens in turn a route to tune the energy of the confined energy levels. Another route to tailor the electronic

spectrum of the dots is to rely on the electronic coupling that can be achieved by vertical coupling of the quantum dots. This vertical coupling is possible due to the vertical alignment driven by the strain-field induced by one quantum dot. Electronic coupling between stacked layers provides more flexibility for wave function engineering in quantum dots, as it is routinely achieved with quantum wells. The stacking of quantum dots corresponds to the transition between artificial atoms to artificial molecules.

The study of intersublevel transitions in quantum dots covers several fields of interest. The first domain is related to the spectroscopy of the nanostructures. The electronic structure of quantum dots can be inferred by several techniques, including interband spectroscopy or transport measurements. Intersublevel transitions, which involve one type of carriers, electrons or holes, bring additional information as compared to interband measurements to understand and to extract the energy diagram of the quantum dots. The polarization selection rules of the intersublevel absorption differ from those of interband absorption or emission: intersublevel transitions can probe excited states which cannot be observed by interband measurements. As will be illustrated below, carrier dynamics and relaxation mechanisms can also be successfully investigated by studying intersublevel transitions.

Intersublevel transitions offer also great opportunities for the development of new devices in the midinfrared. By analogy with quantum well intersubband photodetectors, one of the first device application that has been proposed was the realization of quantum dot infrared photodetectors for infrared detection and imaging. Clearly, one of the anticipated advantage of using quantum dots instead of quantum wells is related to the difference in capture and relaxation mechanisms between the dots and the wells. This should result in an improved responsivity, a lower dark current and an higher operation temperature. Besides, the polarization selection rules for intersublevel absorption differs between quantum dots and quantum wells. Normal incidence operation can therefore be expected with quantum dots. Quantum dots allow also the study of original structures and geometries like lateral quantum dot photodetectors which cannot be investigated with quantum wells.

The purpose of this article is to review the midinfrared properties of self-assembled quantum dots and discuss their interest for the development of quantum dot infrared photodetectors. The article is organized as follows: Section 2 describes the calculation of the quantum dot energy levels in lens-shaped InAs/GaAs self-assembled quantum dots and discusses the infrared intersublevel absorption. Section 3 is devoted to the relaxation in relation with the strong coupling regime for the electron phonon interaction in quantum dots. Section 4 deals with the quantum dot infrared photodetectors.

2. Quantum dot energy levels

2.1. Theoretical electronic structure

2.1.1. Introduction

The theoretical knowledge of the electronic structure of III–V self-assembled quantum dots is a crucial step towards the interpretation and the understanding of the infrared experimental data. The knowledge of the electronic structure is naturally a precious basis for the spectroscopy but also brings valuable theoretical information that cannot be directly accessed experimentally. Because of the three-dimensional confinement, the density of states is delta-like with well energy separated energy levels, instead of being composed of continuous bands or sub-bands of energy levels as it is the case in quantum wells or bulk semiconductors. Depending on the size and geometry, numerous levels can be confined in the conduction band and even more in the valence band. Nonintuitive selection rules, dipole lengths or polarizations can rule the optical transitions between these levels. In the case of two-dimensional heterostructures, a relevant electronic structure can be obtained at a very low computational cost in rather simple single band parabolic envelope function models. As opposed to quantum wells and for many reasons the calculation of the energies of the confined levels, wave functions, and dipole matrix elements in quantum dots is a challenging issue.

On the one hand an exhaustive calculation of the electronic structure should first take into account the specific geometry of the dots and specifically the confinement along the three directions of space, even if the lateral dimensions are ten times longer than along the growth axis. The lack of spatial symmetry in the geometries of the quantum dots usually implies high cost three-dimensional computations. This can be the case for quantum dots with an elongated geometry that presents no continuous nor discrete symmetries. Several electronic bands must be considered because of the large confinement energies. The confinement energies can be 10 times that of quantum wells because of the strong confinement of the carriers along the growth axis and in the layer plane. Non-parabolicity of band diagram of underlying semiconductors used to construct the heterostructure is thus no longer negligible. It results in a correction in the energies of about 30% as compared to what can be expected from a parabolic dispersion and leads to strong band mixing. The electronic structure also depends on the strain field which is present in these lattice-mismatched materials. The strain can be inhomogeneous within the dot, involving not only biaxial components but also nonnegligible shear components. The surrounding of the dot is also strained and can play a significant role on the bound-to-continuum transitions. The effect of strain on core and barrier material band structures should be considered since it

modifies the energy band gaps and lifts up the heavy-light hole degeneracy at the zone center. The piezoelectric field originating from the shear component of the strain should also be taken into account since it changes the level energies. There is also an inhomogeneous broadening of the optical properties of dot ensembles due to the size fluctuation from dots to dots and from one dot plane to another and thus there is the necessity to consider dot of different sizes, shapes and compositions. Coulomb interactions finally can play a nonnegligible role in multi-charged quantum dots.

On the other hand a difficulty comes from a relative uncertainty on the input parameters. Despite numerous experimental characterizations, the exact geometry, the composition, the effect of the In segregation are not perfectly known experimentally. These parameters will depend on the growth conditions and a slight variation on their values (e.g., composition) can lead to strong deviations on the calculated electronic structures (e.g., interband transition energies).

Several theories have been developed to assess the electronic structure of the quantum dots. The simplest and first developed approach is based on the effective-mass theory. Single-band effective-mass calculations have been performed for InAs/GaAs dots with various geometries: cones [14,15], square based pyramids [12,16], thick lenses [17], flat lenses [18]. Note that a simple cubic quantum box model gives very crude predictions on the dipole matrix elements and level energies as compared to those provided by a 3D model which accounts for the realistic geometry of the dots. 3D single band effective mass is often a good compromise if one does not require accurate energy predictions. Otherwise **k**.**p** calculations including 4, 6 and 8 bands have also been performed on square based pyramids [19–25], or flat lens shapes [26,27]. These multiband calculations account for the band-mixing and in particular for the non-parabolicity. Note that microscopic semiempirical pseudopotential methods [28] are limited in the same way as **k**.**p** techniques because of the present lack of accuracy on the input parameters [25].

In the following we present a 3D 8 band **k**.**p** calculation of the confined states in the conduction band and in the valence band of InAs/GaAs quantum dots. A description of the electronic structure, of the polarization and lengths of the dipole matrix elements of the intersublevel transitions is given. The purpose of this calculation is to provide a realistic basis for the interpretation of the infrared properties. Despite the uncertainty on the input parameters, this calculation provides a coherent frame for the interpretation of several of the investigated infrared properties: absorption [27,29,30], photoinduced absorption [18,31], emission [29,32], photocurrent [33], harmonic generation [34–38], with valuable information given on overall electronic structure and matrix elements.

2.1.2. Quantum dot geometry and composition

The InAs quantum dots are grown by molecular epitaxy on [001] GaAs substrate [11]. From structural measurements the dot density is around 4×10^{10} cm^{-2}. In the literature, various geometries for InAs islands grown on GaAs have been reported: thick [39] or flat lenses [11], square-based [40] or elongated pyramids with different facet orientations [13,41]. These geometries mainly depend on the growth conditions. Here the geometry is chosen according to both transmission electron microscopy (TEM) [11] and cross-section scanning tunnelling microscopy (XSTM) structural characterizations [42]. These studies show that the InAs dots grown on GaAs that we have investigated roughly have a lens-shaped geometry with a low aspect ratio of ~ 0.1 (height over diameter) as seen in Fig. 1. Typical heights span the 1.5–2.5 nm range. From XSTM the dot core is found to be constituted of pure InAs with a sharp interface between InAs and the GaAs barrier with a roughness below 0.5 nm [42]. In the calculation, the InAs volume is thus modelled as follows: a portion of a sphere, 2.5 nm high and 25 nm in diameter, lying on the bottom of a 0.5 nm thick wetting layer.

2.1.3. Strain field

Self-assembled quantum dots are strained heterostructures since their Stranski–Krastanow growth mode uses the natural lattice mismatch between the substrate and the deposited material. In the case of the InAs/GaAs couple, this mismatch is around 7% and leads to a strong strain field within and around each quantum dot. The 3D components ε_{ij} of the strain tensor are key parameters on which depends the electronic structure of the bulk underlying materials (InAs and GaAs for the system presented in this article) and thus the electronic structure of the quantum dot. The band gap of InAs is increased by more

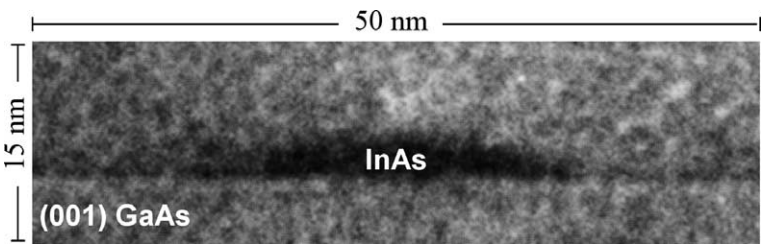

Fig. 1. Cross section image of an InAs quantum dot embedded into a GaAs matrix obtained by Transmission Electron Microscopy (Courtesy of Gilles Patriarche, Laboratoire de Photonique et Nanostructures, CNRS, Marcoussis).

than 100 meV due to a 7% in-plane applied strain as compared to unstrained InAs. The heavy-light hole degeneracy at the zone center is also strongly lifted pushing the light hole band around 200 meV beneath the heavy hole band. As compared to quantum wells one *a priori* expects the presence of non-vanishing 3D shear components because of the 3D nature of the quantum dot geometry. This component is at the origin of a piezoelectric field that can be nonnegligible, especially in the case of high aspect ratio islands [25].

The strain field can be calculated by minimizing the strain energy E_{strain} given by a valence force field theory [43]:

$$E_{\text{strain}} = \sum_{i}^{\text{All atoms}} \left(\sum_{j=1}^{4} \left(\frac{3}{8}\alpha_{ij} \frac{(r_{ij}^2 - r_{0,ij}^2)^2}{r_{0,ij}^2} + \sum_{k>j}^{4} \frac{3}{4}\beta_{ijk} \frac{(\vec{r}_{ij}\cdot\vec{r}_{ik} - \vec{r}_{0,ij}\cdot\vec{r}_{0,ik})^2}{\vec{r}_{0,ij}\cdot\vec{r}_{0,ik}} \right) \right). \tag{1}$$

In this microscopic theory the strain energy is expressed from the variation of the bond length and bond angles for all the atoms within the deformed zinc-blend lattice. In Eq. (1) $\vec{r}_{ij}$ is the vector going from atom i to atom j, $\vec{r}_{0,ik}$ the vector from atom i to atom k in the unstrained crystal, the indexes j and k designing one of the four nearest neighbour of atom i. Taking into account the strain limit conditions set by the substrate, the minimization gives access directly to the displacement of the atoms at an interatomic length scale, in particular around the hetero-interfaces, respecting the $\underline{4}3$ m symmetry of the crystal and depending solely on the chosen dot geometry and local dot and barrier compositions. One will note that, for each material InAs or GaAs, there are only two input coefficients (bond stretching α_{ij} and bond-angle bending β_{ijk}) to generate the macroscopic elastic properties given by three independent elastic constants. In practice for InAs/GaAs the main two lattice constants (C_{11}, C_{12}) are fitted exactly at the expense of the third less important one (C_{44}) fitted with an acceptable 10% error. C_{44} is involved in the shear component of strain and plays a lesser role for flat geometries.

Fig. 2 depicts a representation of the strain field of one flat lens-shaped pure InAs self-assembled quantum dot floating over a 0.5 nm thick InAs wetting layer and inserted into a zinc-blend GaAs matrix. For a height of 2.5 nm and a base diameter of 25 nm the calculation shows that the volume dilation $\varepsilon_{xx} + \varepsilon_{yy} + \varepsilon_{zz}$ is essentially localized into the InAs volume while the

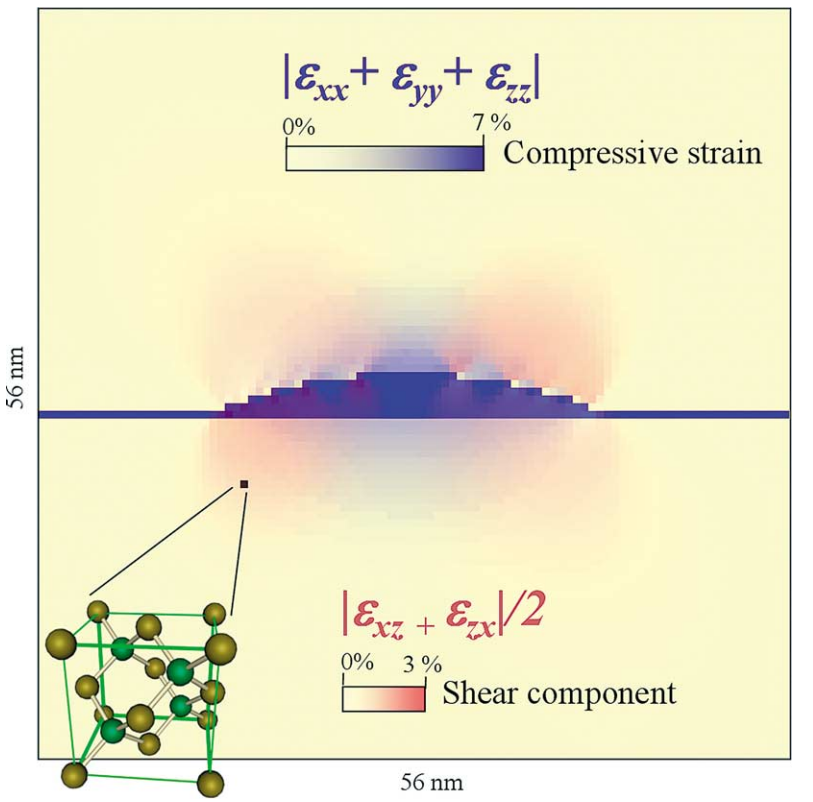

Fig. 2. Compressive and shear components of the strain field in an InAs/GaAs self-assembled quantum dot calculated by minimizing the strain energy given by a microscopic valence force field theory. The compressive component (blue) is roughly piecewise constant and located into the InAs volume and mimics the strain of a thin InAs quantum well. The nonnegligible shear component corresponds (red) to less than 3% of lattice deformation.

GaAs barriers remain nearly unstrained. A more detailed analysis shows that the strain tensor is close to the one of a thin InAs quantum well grown on GaAs: the relative elongations are nearly piecewise constant (i.e., nearly constant in the InAs volume and nearly constant in the GaAs volume) and the shear component is only moderate near the interfaces. The main reason for this specificity is the small aspect ratio (0.1) of the dot. One also expects much smaller piezoelectric field in this flat dot than for high aspect ratio geometry [15]. In quantum dots exhibiting a higher aspect ratio, the piezoelectric potential may lead to significant corrections (∼10 meV) to the level energies [12]. In what follows we will consider that the strain field is biaxial piecewise constant and we will neglect the effect of piezoelectricity on the level energies.

2.1.3.1. Three-dimensional 8 band k.p resolution of the Schrödinger equation The theoretical electronic structure of one quantum dot, i.e., the confined level energies and wave functions, is provided by the three-dimensional resolution of the Schrödinger equation (2) written in a 8 band **k**.**p** formalism taking into account a realistic flat-lens shaped geometry for the quantum dot. The base of the InAs lens is deliberately 10% elongated along the [$\underline{1}$10] direction to account for spectroscopic data. The Pidgeon–Brown Schrödinger equation is written [44]:

$$\left(\widehat{H}_{kp8} + \widehat{H}_{\text{strain}} + \widehat{V}\right)\chi(\vec{r}) = E\,\chi(\vec{r}), \tag{2}$$

where $\widehat{H}_{kp8}$, $\widehat{H}_{\text{strain}}$, $\widehat{V}$, $\chi(\vec{r})$, E are the unstrained 8 band **k**.**p** Hamiltonian matrix containing 168 real in-space acting operators, the strain Hamiltonian, the confining potential, the envelope wave function of the eigenstate and the energy respectively. The 8 bands include the conduction band, the heavy hole, light hole and spin-orbit split-off bands with a quantized spin along the growth axis. This formalism is a well-known and powerful mean to describe accurately the band structure of bulk semiconductors near the zone center. It is used here along with the envelope function theory [45] to extract a realistic description of the nanostructure states. The 8 band **k**.**p** matrix operator takes into account the valence band mixing, valence-conduction band coupling at the origin of the non-parabolicity of the dispersion relation and strain effects. The strain field is biaxial with an in-plane deformation imposed by unstrained GaAs barriers. The resolution of the Schrödinger equation gives access to the confined level energies E and 3D envelope wave functions $\chi(\vec{r})$ from which all the matrix elements are extracted. For the infrared data analysis, we consider specifically intersublevel transitions between either conduction states or valence states. The dipole lengths as well as the polarization of the transitions (in the layer plane, along the growth axis) are key parameters with the transition energies that enable to disentangle the infrared experimental data.

2.1.4. Resolution

The 8 band **k**.**p** 3D Schrödinger equation is solved numerically by finite difference or finite element discretization on a typically $70 \times 70 \times 50$ uniform parallelepiped cell grid. The dot and the wetting layer volumes are encompassed into a large infinite wall box ($40 \times 40 \times 14$ nm^3) in order to limit the size of the discretized Hamiltonian and to impose null or periodic wave function conditions at the edge of the box. The confining box is chosen large enough so that the energy of the states confined within the dot remains nearly unaffected by a change of the box dimension. The resulting finite rank Hamiltonian matrix is then partially diagonalized using a customized iterative block Jacobi–Davidson algorithm [46] implemented in *Javel*, the C++ Schrödinger computation program compiled on a 1 GHz processor Personal Computer. The program is stopped when the vector residual normalized by the eigenenergy reaches a lower enough threshold of 10^{-6}. The algorithm allows the determination of up to 100 first confined state energies and their associated wave functions from which are extracted the dipole matrix elements (length, polarization) and Coulomb interaction energies of the intersublevel transitions.

Note that from a mathematical and numerical point of view the resolution of the Schrödinger equation is not straightforward. As far as finite difference is concerned, there are well known and systematic methods applied for parabolic or elliptic differential equations. Unfortunately the 8 band **k**.**p** Schrödinger equation is hyperbolic and such systematic approach is not available. The simultaneous search for consistence and numerical stability of the discretization schemes can be very tedious. Even when the mathematics of the discretization schemes is clear, there are still numerical issues related to the diagonalization of the large rank (10^6–10^7) matrix, choice of preconditionners and efficient extraction of eigenvalues and eigenvectors interior to the matrix spectrum.

2.1.5. A simple view of the electronic structure

It is instructive to first consider the electronic structure given by a cubic quantum box with infinite barrier heights. In this case, the electronic structure results from the independent combination of the states of infinite wall quantum wells of respective widths L_x, L_y, L_z along the three x, y and z directions. If the carrier is in a parabolic single band described by the scalar effective mass matrix (m_{xx}, m_{yy}, m_{zz}) then the level energies have the simple following form:

$$E = \frac{\hbar^2\pi^2}{2}\left(\frac{n_x^2}{m_{xx}L_x^2} + \frac{n_y^2}{m_{yy}L_y^2} + \frac{n_z^2}{m_{zz}L_z^2}\right) \tag{3}$$

and the envelope wave functions the form:

$$\chi_{n_x,n_y,n_z}(x,y,z) = \frac{2^{3/2}}{\sqrt{L_x L_y L_z}} \sin\left(n_x \frac{\pi}{L_x} x\right) \sin\left(n_y \frac{\pi}{L_y} y\right) \sin\left(n_z \frac{\pi}{L_z} z\right), \tag{4}$$

where n_x, n_y, n_z are positive nonnull integers. One interest of this simple model is to show that the states can be sorted by the numbers of the wave function nodes n_x, n_y, n_z along the three directions of space. According to this notation, the ground state is labelled 000, the first excited state resulting from the confinement along the x-axis is 100 and so on. Allowed optical intersublevel transitions between level i and j ($\langle \chi_i | \vec{r} | \chi_j \rangle \neq 0$) only exist between states of odd difference quantum numbers along the same axe, e.g., 000 → 100, 100 → 200, 000 → 300 but not 000 → 200, 100 → 001, etc. In a non-cubic quantum box, a convention is to label the states from the denomination they would have in the cubic dot obtained by continuously deforming the original dot.

2.1.6. A more sophisticated view

Fig. 3 depicts the electronic structure of one InAs/GaAs self-assembled quantum dot as deduced from the 3D resolution of the 8 band **k**.**p** Schrödinger equation. Note that this picture forms a base from which polaronic structure (discussed in the next section) can be understood. In what follows we will forget the spin since all the states are doubly spin degenerated. The ground

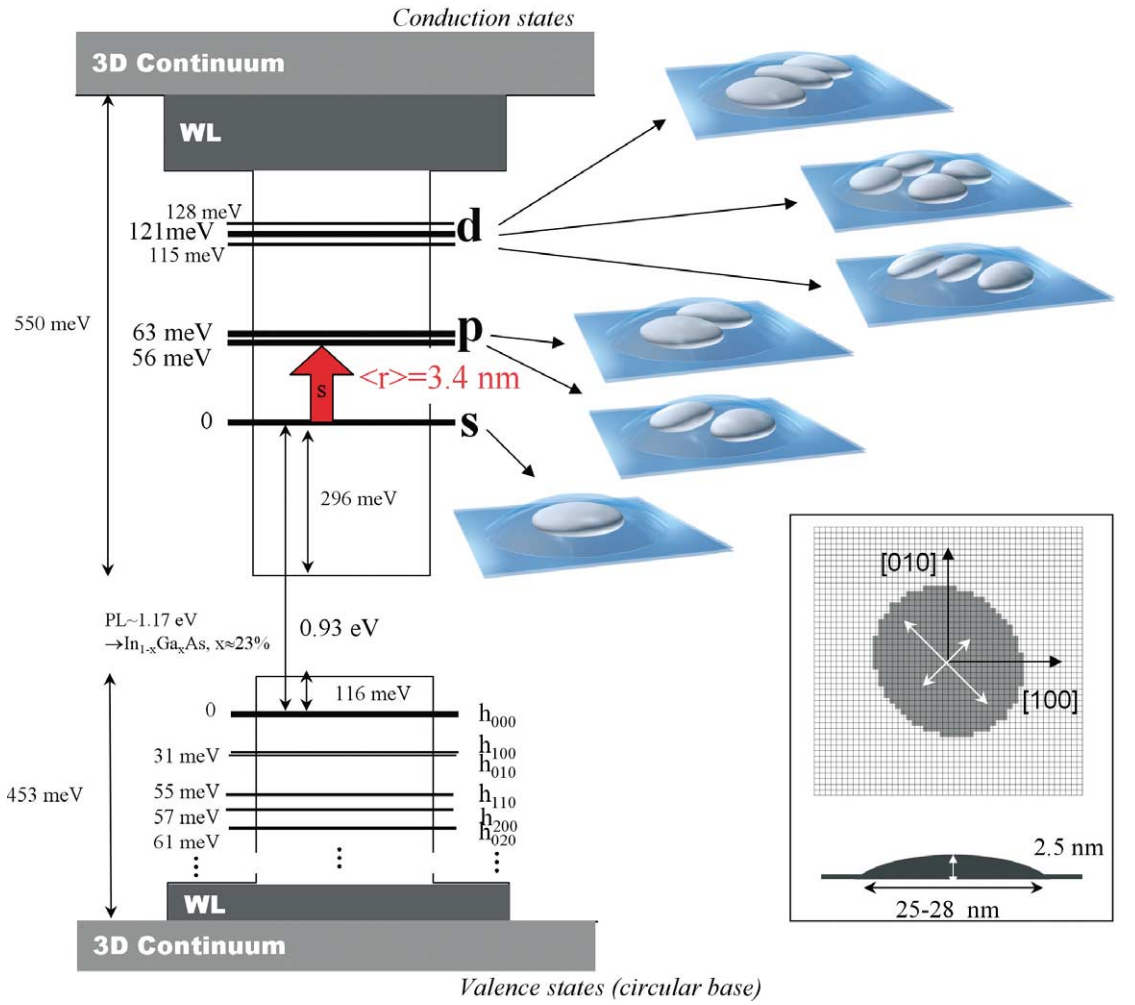

Fig. 3. Electronic structure of a InAs/GaAs self-assembled quantum dot as deduced from the 3D resolution of the Schrödinger equation written in a 8 band **k**.**p** formalism. The resolution takes into account a realistic elliptical flat lens-shape geometry ($25 \times 28 \times 2.5$ nm^3) described in the inset. The representation of the envelope wave functions considers probability volumes including 2/3 of the presence probability of the electron. WL denotes the wetting layer 2D continuum, beneath the bulk barrier 3D continuum.

state is located around 300 meV above the InAs band edge as a result of the strong confinement along the three directions of space. The confinement comes essentially from the growth axis. The envelope wave function is s-like so this state is called the s state instead of e000. Note that because of the strong confinement energy this conduction state is constructed using the non-parabolic part of the band structure of InAs and GaAs and that 10% of the square envelope function is projected onto the valence basis. The wave functions of the first two electronic excited states are p-like and thus are referred to as the 'p' states instead of e100/e010. The splitting between the p states originates from the elongated geometry and the slightly stronger confinement along [110] than along [−110] crystal direction. The s–p transition is predicted at 56 and 63 meV corresponding to wavelengths around 20 μm. The s–p transition is a model of intersublevel transitions in semiconductor quantum dots. It is well isolated from other transitions, it occurs between well confined levels far from the continua, it has a large oscillator strength with a predicted dipole length as long as 3.4 nm and is fully polarized in the layer plane. At higher energy the energy spectrum contains 3 highly excited discrete states, called the 'd' states (corresponding in a cylindrical symmetry quantum dot to two '1d' and one '2s' states). The other calculated states lie above the wetting layer energy and their wave functions appear to be delocalized. As a matter of fact these states are the first ones of a set of states either delocalized in the wetting layer (subband-like states) or three-dimensionally delocalized around the dot (bulk-like states). They belong to what will be respectively called in the following the continuum of the wetting layer and the continuum of the GaAs barriers. Naturally these states, which strongly depend on the choice of the large confining box used to solve the equation, become even better approximations of the states of the continuum when the size of the large box increases towards infinity. The onset of the wetting layer continuum, i.e., the energy of the first states starting to delocalize into the wetting layer, is around 30 meV below the GaAs band edge or equivalently 120 meV above the ground state. Note that as far as the conduction states are concerned, no level e001 corresponding to the confinement along the growth axis is predicted to be confined. This is confirmed experimentally, the main reason being the too strong confinement along the growth axis (the height of the quantum dot is 2.5 nm).

In the valence band, despite the smaller barrier height a much larger number of states are confined because of the heavier effective masses. Only the very first states are represented in Fig. 3. The confinement energy of the ground state h_{000} is also smaller than in the conduction band. From a general point of view, the valence electronic structure is more complex than the conduction one. However good qualitative agreement can be found with linear (see, e.g., [29]) and non linear infrared spectroscopy (see, e.g., [36,37]).

2.1.7. Size dependence

The energy of the confined levels increases when the dot size decreases (not shown). A stronger confinement leads to a blue-shift (red-shift) of the energy of the bound-to-bound transitions (bound-to-continuum transition). For instance 10% size variation corresponds to 3.5 meV shift of the s–p transition. The bound-to-continuum transitions red-shifts for smaller size because the confinement energy of the confined states increases while the continuum energy is hardly affected by the change of the dot volume. 10% size variation induces a 24 meV shift on these bound-to-continuum transitions.

2.1.8. Interaction energy

In the situation where more than one carrier are captured into the dot, one a priori must take into account Coulomb interaction and form many particle states. The direct energy J and the exchange energy K are:

$$J_{ij} = \iint \frac{|\chi_i(r_1)|^2 |\chi_j(r_2)|^2}{\varepsilon |r_1 - r_2|} \,\mathrm{d}r_1 \,\mathrm{d}r_2, \tag{5}$$

$$K_{ij} = \iint \frac{\chi_i(r_1)\chi_i^*(r_2)\chi_j^*(r_2)\chi_j(r_1)}{\varepsilon |r_1 - r_2|} \,\mathrm{d}r_1 \,\mathrm{d}r_2, \tag{6}$$

where ε the dielectric permittivity and i and j denote the state of the two carriers in interaction. For two electrons confined into the dot, the Coulomb interaction energy is, in the Hartree–Fock approximation, $J_{\mathrm{s–s}} = 26.4$ meV. The excitonic binding energy of one electron–hole pair captured into one dot is $K_{\mathrm{e–h}} - J_{\mathrm{e–h}} = -31.3$ meV in the same approximation. These quantities are much smaller than the confinement energy and, in first approximation, can be neglected.

2.2. Infrared absorption spectroscopy

The measurement of the infrared absorption is the most direct path to observe intersublevel transitions in quantum dots. Absorption usually results from the transition of carriers from the ground state of the dot, either in the conduction band or in the valence band, towards an excited state. For the InAs/GaAs self-assembled quantum dots, the absorption associated with the intersublevel transitions occurs in the midinfrared and in the far infrared spectral range. Intersublevel absorption spectroscopy is a powerful technique to get access to a very detailed experimental description of the electronic structure of the dots. We emphasize that intersublevel absorption spectroscopy is very complementary to interband spectroscopy such

as photoluminescence. Intersublevel absorption corresponds to a unipolar measurement since it only involves one type of carrier (electron or separately hole) while interband transitions involve confined excitons. Infrared absorption spectroscopy directly provides the difference between confinement energies (i.e., without any difference associated with the exciton binding energy). In addition, intersublevel absorptions satisfy distinct transition rules as compared to interband transitions. An interband transition essentially follows the overlapping integral between envelope functions of the initial and final state while an intersublevel transition is governed by the dipole matrix element between the initial and the final envelope wave functions. Intersublevel absorption may therefore give access to states that are not observed in interband measurements. At last the information on polarization allows a fine tracking of the main origin of the excited levels (in-plane confinement, growth axis confinement).

Beyond the fundamental study of the electronic structure, intersublevel absorption opens the route to the realization of quantum dot infrared photodetectors. For this particular application, one specific advantage of the quantum dots is the relaxation of the polarization selection rules as compared to two-dimensional heterostructures. In quantum wells it is well known that, at least in the conduction band, intersubband transitions are always polarized along the growth direction [47]. This polarization selection rule prevents any absorption at 'normal-incidence', thus implying additional technological steps to couple the infrared light to the intersubband dipole. On the contrary, because of the three-dimensional confinement, the intersublevel transitions in 0D systems are expected to be polarized either along the growth axis or in the layer plane. The in-plane polarization of the intersublevel transitions results from the in-plane confinement of the carriers. In the case of self-assembled quantum dots, the first observation of intersublevel absorption was reported by Drexler et al. in 1994 in the conduction band of electrically charged InGaAs quantum dots [30]. The electronic transition between the *s* ground state and the first *p* excited state was found resonant at 41 meV.

2.2.1. Infrared absorption

Fig. 4 reports the mid and far infrared absorption of *n*-doped InAs/GaAs self-assembled quantum dots measured by Fourier transform spectroscopy. The dots are populated by inserting a Si doping plane 2 nm beneath the wetting layer. The sheet doping density is nominally chosen to correspond to 2 and 1.5 electrons per dot in the samples of the left and right-hand side of the figure, respectively. Two different configurations are used.

On the left-hand side, the absorption is measured in a normal incidence configuration in a sample containing 30 quantum dot planes separated by 50 nm GaAs barriers. The temperature is 5 K and the polarization is set along either cleaved edge directions. Two clear infrared resonances are observed at 56 and 63 meV. The full width at half maximum is 6 meV. Following

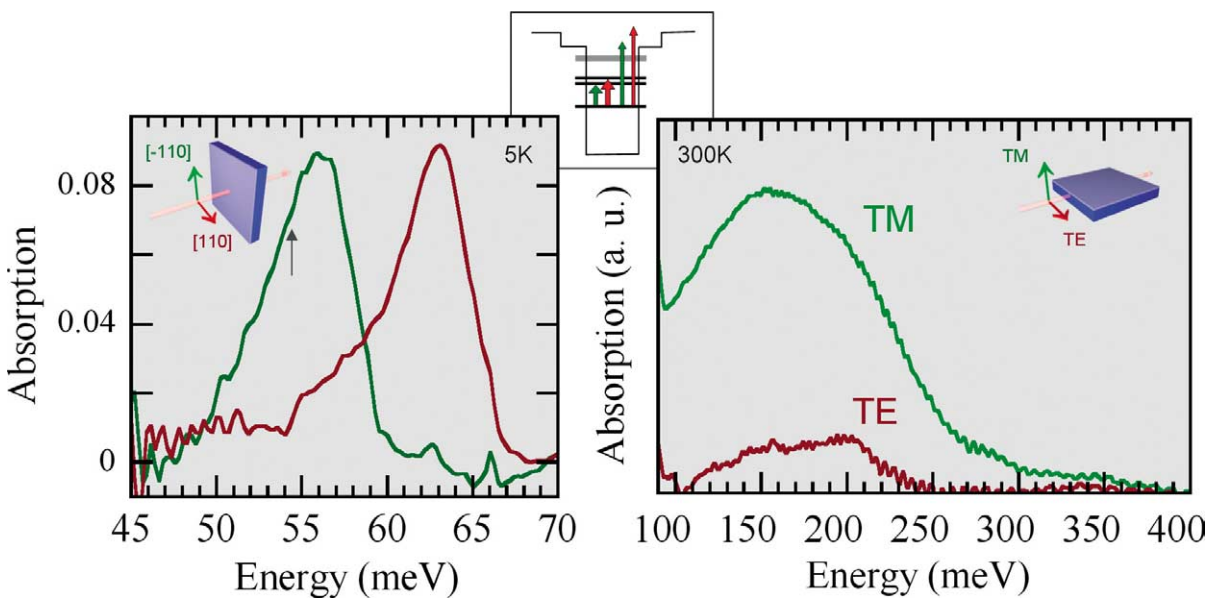

Fig. 4. Infrared absorption of *n*-doped InAs/GaAs self-assembled quantum dots at 5 K and 300 K in two different configurations. On the left-hand side, the normal incidence configuration probes the in-plane polarized s–p intersublevel transition for two mutually orthogonal polarisations. On the right-hand side, the resonant absorption of the transition of the electrons towards the continua is probed in a wave guide configuration for a TE and TM polarizations. As opposed to the conduction band of quantum wells, clear and strong in-plane polarized absorptions are observed, both for bound-to-bound and bound-to-continuum transitions.

the calculated electronic structure, these infrared resonances are attributed to the intersublevel transitions of the electrons from the s ground state to the p excited state. The exact agreement (within less than 1 meV) between the predicted transition energies and the experiment is fortuitous but demonstrates an overall validity of the model and the input parameters. In particular the observed 7 meV s–p splitting energy agrees with a 10% elongation of the dot along the [−100] direction. The broadening of the absorption is attributed to the size fluctuation of the dots. According to the multiband 3D simulation, the observed broadening corresponds to a ±9% dot size fluctuation in good agreement with structural characterizations.

On the right-hand side of Fig. 4, the absorption is measured in the 90–400 meV energy range in a wave guide configuration. The sample contains 40 quantum dot planes inserted into the core of a GaAs/$Al_{0.9}Ga_{0.1}As$ midinfrared waveguide. The light is injected with an infrared microscope coupled to the Fourier transform spectrometer. Polarization can be set either TE, in the layer plane, or TM along the growth axis. In this configuration, spectrally large infrared resonances are observed around 8–10 μm wavelength. In TM polarization, the absorption is maximum at 155 meV with a ∼100 meV full width at half maximum. In TE polarization, the absorption is maximum at 200 meV with the same width. Considering the theoretical electronic structure, the TM resonance is attributed to the bound-to-continuum absorption from the s ground state to the delocalized state of the wetting layer continuum. The polarization is reasonable since the expected transfer of charge (i.e., the dipole) is mostly along the growth axis from the dot to the wetting layer. The TE resonance on the contrary is attributed to the transition towards the bulk GaAs barriers, at a slightly higher energy. The 45 meV difference between the TE and TM resonances corresponds roughly to the wetting layer subband depth and, as compared to the calculation, integrates the fact than the oscillator strength of a bound-to-continuum transition is maximum at higher energy than the continuum onset [45]. The 100 meV broadening of the absorption is attributed to three factors: the dot size fluctuation, the bound-to-continuum nature of the transition, and a possible contribution of the d-states around 120 meV (in TM polarization).

2.2.2. Absorption cross section

The absorption $\alpha = \sigma n$ of an intersublevel transition results from the product of the absorption cross section σ of the transition and of the number of involved carriers n. The absorption cross section reflects the oscillator strength of the transition through its squared dipole length dependence:

$$\sigma = \frac{E}{HWHM}\frac{\mu^2}{\hbar n c \varepsilon_0}, \tag{7}$$

where E, μ, $HWHM$ are the transition energy, the dipole and the half width at half maximum. $\hbar$, $n = 3.3$, c, and ε_0 are the reduced Plank, refractive index, light speed and vacuum permittivity constants. The average dot population can therefore be deduced from the measurement of the absorption amplitude (8.8% for 30 quantum dot planes) and the theoretical 3.4 nm dipole length for the s–p transition. At low temperature 1.2 electrons are estimated to be transferred from the doping center. Note that the average dot population strongly depends on temperature. At room temperature only 0.3 carrier is confined per dot, the remaining electrons being essentially thermally excited into the continua [26].

Regarding the bound-to-continuum transitions, the cross section can be inferred from a detailed analysis of the amplitude of the absorption [48]. Absorption cross section of the order of 2×10^{-14} cm^2 is reported in photodetector samples [33]. Note that the TM absorption is much stronger than the TE absorption. This is not surprising. For a polarization in the layer plane, the oscillator strength is essentially concentrated into the bound-to-bound s–p transition. On the contrary no level of the type e001 is confined in the dot. The oscillator strength along the growth axis is therefore concentrated solely in the bound-to-continuum transition.

3. Polaron relaxation

3.1. A paradigm change: from weak coupling to strong coupling

The relaxation processes in semiconductor quantum dots have been debated for more than a decade now since the first prediction by Bockelmann and Bastard in 1990 of a quenching of the relaxation of carriers in zero-dimensional nanostructures [3]. In the first years that followed, the relaxation mechanisms were discussed based on the idea of a phonon bottleneck [49]. LO phonon emission is a very efficient relaxation mechanism in III–V bulk semiconductors or quantum wells. It leads to relaxation times towards the band edge of no more than a few picoseconds. It was expected however that the discrete nature of the density of states in quantum dots would hamper relaxation by emission of one LO phonon if the carrier energy jump is not equal to the LO phonon energy (36 meV in GaAs). Several alternative mechanisms were proposed to explain the yet relatively fast observed relaxation times: multi-phonon emission assisted by acoustic and/or optical phonon or Auger-type relaxation processes at high carriers densities [50,51]. In any case the interaction of the carriers with the LO phonon thermostat, in terms of phonon emission and Fermi golden rule application, was considered in a weak coupling regime.

Only recently Inoshita and Sakaki suggested that the Fröhlich coupling between a confined electron and the LO phonon bath should not be considered in a weak interaction picture where the electron wave function 'dissolves' itself into the phonon continuum [52]. Instead they inferred from the three dimensional confinement in quantum dots that *the electron and the phonons are strongly coupled* leading to the formation of a bipartite electron–phonon particle in itself (polaron). Provided that the coupling strength is larger than the continuum width, the coupling leads to continuous Rabi oscillation of the electron, i.e., everlasting emission and absorption of one LO phonon. The interaction with the LO phonons can thus no longer be regarded as an electron leaving its state by irreversibly emitting a phonon through the Fermi golden rule. Another way to grasp the origin of this strong coupling is to note that the LO phonon continuum is almost monochromatic and that the electron will only see a particular linear combination of phonons [53]. The coupling can thus be viewed as the coupling between one discrete electron state with a nearly single isolated phonon level, leading to Rabi oscillations of the electron. Very recently the polaronic nature of conduction states in n-doped InAs/GaAs self-assembled quantum dots has been evidenced experimentally using magnetospectroscopy in the far infrared of the s–p transition [54].

Electron relaxation should thus be considered in this polaron picture, i.e., *not* in a *separated* electron/phonon space. In this picture, the polaron is a *stable* eigenstate of the Hamiltonian, the electron performing everlasting Rabi oscillation between the mixed states. Relaxation should therefore not occur. However due to the anharmonicity of the lattice forces, a LO phonon disintegrates in a very short time. In GaAs the LO phonon population decays with a 7 ps time constant at low temperature [55,56]. In practice it is therefore expected that the finite lifetime the LO phonon causes the polaron relaxation [57]. Because of the instability of its phonon component, the polaron exhibits a relaxation triggered by its one-phonon part.

We present in what follows the first experimental evidence of the polaron relaxation in self-assembled InAs/GaAs quantum dots [27]. To identify the related decay mechanism the polaron relaxation time is measured by pump-probe spectroscopy around 20 μm wavelength as a function of the excited state energy and from 5 K to room temperature. The pump source is provided by the free-electron laser CLIO (Centre Laser Infrarouge d'Orsay). We show that the measured relaxation times originate from the polaronic nature of the excited states. Our experimental data support that even at detuning from the phonon energy as large as 19 meV the relaxation occurs and is triggered by the spontaneous disintegration of the optical phonon component into two acoustic phonons.

3.2. A simple polaronic picture

Let us consider a simple description of the polaron states that enlightens the experiment. The interaction scheme is depicted in the left hand side of Fig. 5. If one considers only the one LO phonon modes $|0\rangle$ and $|1\rangle$, containing zero and one phonon respectively and only the $|s\rangle$ and $|p\rangle$ electron levels, the strong coupling of the p zero-phonon states and the s one-phonon state forms two polarons $|+\rangle$ and $|-\rangle$ [53,58]. A simple expression for the polaron eigenstate is given by the coherent superposition $\alpha|s\rangle \otimes |1\rangle + \beta|p\rangle \otimes |0\rangle$ with normalized complex weights α and β satisfying $|\alpha|^2 + |\beta|^2 = 1$. Far away from the energy of

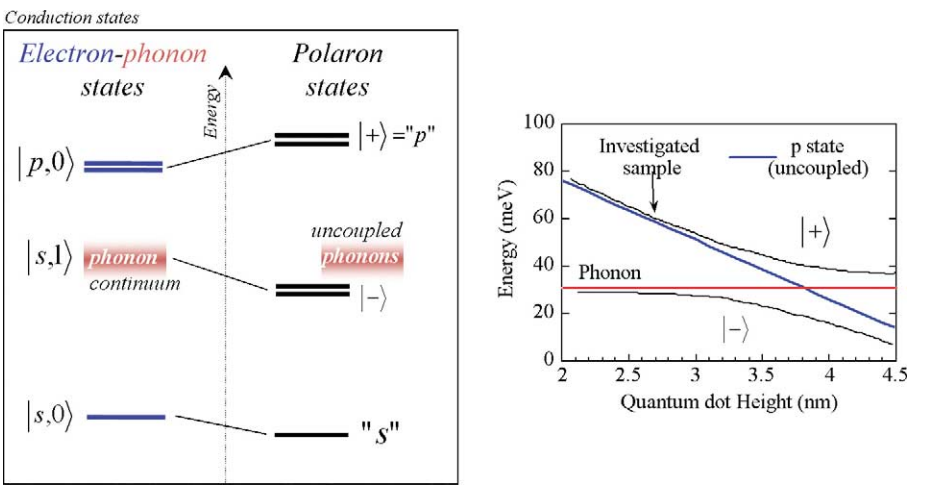

Fig. 5. Left: schematic polaronic structure of self-assembled InAs/GaAs self-assembled quantum dots originating from the strong coupling of confined electronic s and p states and the one LO phonon continuum. Right: energy of the polaron states as a function of the dot size. The anti-crossing corresponds to a polaron with an electron and phonon component of equal weight. Mixing of the electronic p-state to the phonon mode depends on the p state energy as compared to the phonon resonance. The mixing is maximal at the anti-crossing where the electron and phonon weight is equal. For the investigated n-doped quantum dots (vertical arrow), the p state is more electronic than phononic.

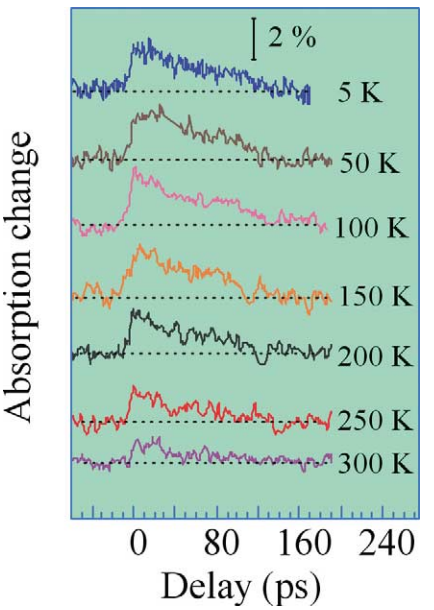

Fig. 6. Transmission modulation of n-doped InAs/GaAs quantum dot absorption as a function of the pump-probe delay. The wavelength of the free-electron laser is set at 22.7 μm near the maximum of the 's–p' transition absorption in Fig. 4.

the optical phonon, polaron type corrections on the confined s and p electron state energies are small. As seen in the right-hand side of Fig. 3, the theoretical correction on the s–p intersublevel electron transition is only a few meV. It also means that the weight α of the phonon part in the $|+\rangle$ state is small for the investigated sample. For this reason the $|+\rangle$ is also labelled 'p' since it is close to a pure electron $|p\rangle$ state. In the same way, the $|-\rangle$ state is essential phononic and we will forget it for now on. The electron s ground state is nearly unchanged by the coupling and remains electronic in nature in first approximation. We will continue to label it 's'. The infrared absorption reported in Fig. 4 (left) is therefore a spectroscopy of the s–p *polaron* transition and the word electron should be exchanged with the word polaron in the infrared spectroscopy discussion (with all other conclusions still holding).

3.3. Pump-probe spectroscopy

The wavelength of the free electron laser CLIO, tunable in a large infrared spectral window 3–120 μm, is set at 22.7 μm near the low energy side maximum of the s–p polaron transition in Fig. 4. CLIO provides high power picosecond pulses suitable to saturate the transition [59]. In a nearly normal [001] incidence configuration the pump and probe beams are focused onto the sample surface with a spot size around 300 μm and spatially separated thanks to the 20° angle between them. Fig. 6 reports the variation of transmission as a function of the pump-probe delay for temperatures spanning the 5–300 K range. At zero delay, a clear saturation of the absorption is evidenced. The partial bleaching is followed by the reconstruction of the absorption verifying roughly an exponential decay with a $T_1 = 70$ ps time constant at 5 K. This decay is attributed to the relaxation of the polaron initially in the laser excited p state towards the s ground state. This result clearly shows that the polaron has a finite relaxation time and is not a stable entity. Note however that this relaxation time is one to two orders of magnitude longer than the relaxation time of electrons in quantum wells or bulk GaAs [27]. We show that it is a consequence of the strong coupling in the nanostructure.

3.4. Relaxation mechanism

In order to analyze the mechanism at the origin of the relaxation, the decay time is measured as a function of the energy by tuning the free-electron laser wavelength across the absorption resonance. Because of the inhomogeneous broadening of the s–p transition, wavelength tuning amounts to probing different dots with different s–p transition energies. As reported in the left-hand side of Fig. 7, the closer to the phonon resonance, the shorter the decay time. This dependence is qualitatively expected from the idea of a polaron relaxing with the disintegration of its phonon component. The closer to the phonon resonance, the larger the phonon weight in the polaron state and the quicker the relaxation occurs since the probability of the disintegration varies with $|\alpha|^2$. To support quantitatively this idea, the polaron relaxation time is calculated using the non perturbative treatment

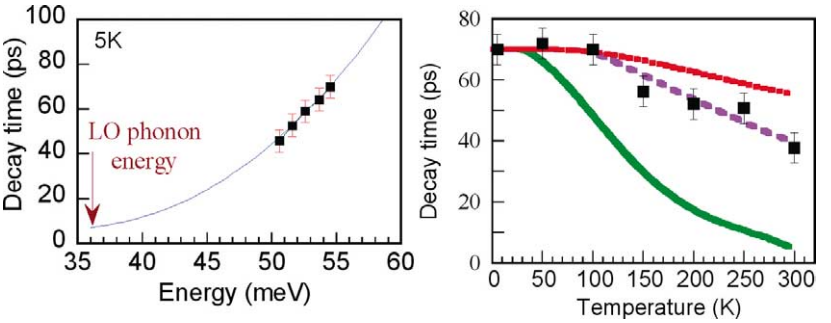

Fig. 7. Left: measured decay time as a function of the probed transition energy. The decay time becomes shorter as it gets closer to the LO phonon energy. As seen using the model of [57] (solid line) the dependence is understood in the polaron picture where the polaron relaxes because of the disintegration of its phonon part into two acoustic phonons. Right: the relative temperature 'robustness' of the relaxation time is attributed to the only slight decrease of the LO phonon lifetime at room temperature (5 ps) as compared to its value at 5 K (7 ps) as shown by the agreement with the sensible theoretical dotted line. This line assumes a constant phonon lifetime of 7 ps up to 100 K and then a linearly decreasing lifetime down to 5 ps at 300 K. The other two thick lines correspond to a model where the phonon lifetime is constant (7 ps, upper line) or follows the temperature dependence of [56] (lower line).

of Li et al. and reported as a full line in the plot [57]. The agreement with the experimental data is obtained with only the coupling strength as a fitting parameter (4.4 meV) and therefore the polaron decay is attributed to the disintegration of the phonon part, here into two acoustic LA phonons.

To further support this polaronic picture, the temperature dependence of the relaxation time (right-hand side of Fig. 7) is also compared to the model of [57]. The striking feature is the still long decay time measured at room temperature (37 ps). But again this is not surprising. In the simulation the LO phonon lifetime at low temperature is 7 ps (i.e., the low temperature GaAs measured value) [55]. The phonon lifetime is slightly shorter at room temperature. In bulk GaAs this value is down to 3.5 ps [60]. Assuming instead a lifetime of 5 ps at 300 K (dotted line in the right-hand side of Fig. 7), a good agreement is again found with the experimental data. Note that 5 ps is a sensible time since the involved phonons are related to InAs quantum dots and not to bulk GaAs.

There has been other detailed theoretical analysis of the polaron relaxation in InAs/GaAs self-assembled quantum dots, in particular using microscopic Hermitian approach [53,54] and including the treatment of quantum dot molecules [61] and extended to the excitonic polaron [62,63]. In these cases it is predicted that the relaxation occurs only in a narrow window (± 8 meV) around the phonon resonance. Our experimental data are not compatible with this model since relaxation is observed even far away ($\sim$19 meV) from the phonon resonance. This discrepancy is very likely related to the phonon instability mechanism chosen in the microscopic model for the phonon disintegration, namely disintegration of a zone center LO phonon into one band edge LO phonon and one TA acoustic phonon [64]. Considering instead a disintegration into two acoustic LA phonons in the microscopic model of [53] should enable theoretically the polaron to relax at $\sim$54 meV, the energy corresponding to our measurements.

3.5. Conclusion

The main idea that is worth conveying is that the *polaron picture* is the correct way of describing electron relaxation in InAs/GaAs self-assembled quantum dots. The relaxation should no longer be addressed in terms of irreversible emission of LO phonons because these phonons are in strong coupling with the electrons. Beyond the fundamental importance of the measurements of these relaxation times and the understanding of the related mechanisms, the relaxation has a significant impact on the performances of quantum dot based optoelectronic devices. In quantum dot infrared photodetectors, the efficiency of the carrier recapture into the dots limits for instance the temperature range for a background limited operation of the device. Only bound-to-bound state relaxation is presented here and both theoretical and experimental efforts should continue to be devoted to the relaxation processes in quantum dots, in particular those involving transport and capture from the wetting layer and barrier continuum.

4. Quantum dot infrared photodetectors

4.1. Principle of operation

The principle of operation of *vertical* quantum dot infrared photodetectors (QDIPs) is very similar to that of quantum well infrared photodetectors (QWIP) [2]. Such infrared photodetectors correspond to photoconductors with semiconductor quantum

wells as the optically active region. The generation and recombination of the carriers is therefore localized. This feature leads to a distinction between QWIPs and conventional photoconductors where generation and recombination of the carriers are homogeneously distributed. The absorption of the infrared light is based on the intersubband absorption process. A typical QWIP structure consists of 50 periods of GaAs quantum wells separated by AlGaAs barriers. The active region is embedded between two heavily doped n^+ regions that provide the ohmic contacts. The quantum wells are intentionally doped. For a given detection wavelength, the size of the wells and the composition of the barriers can be adjusted in order to tune the energy of the first confined subband close to the bottom of the conduction band of the barrier. This provides a nearly resonant intersubband transition with a large oscillator strength. Under infrared illumination, the carriers are photoexcited from the ground state of the well to the edge of the conduction band of the barrier. Under an applied electric field, the carriers can either be captured in the well or be collected and diffuse to the barriers. Following the absorption and the collection of carriers from the quantum wells, carriers are emitted from the contact layers in order to refill the well, which leads, in turn, to an increase of the photocurrent.

The QWIPs provide several advantages for infrared imaging applications as compared to standard HgCdTe technology. QWIPs are usually based on GaAs and take advantage of the processing advances obtained for this mature technology. QWIPs structures can be grown with good uniformity on large wafers using standard techniques like molecular beam epitaxy. High-performance thermal imaging can therefore be achieved on large array sizes. The noise equivalent temperature difference (NEDT) that can be achieved is of the order of 10–40 mK. This parameter characterizes the temperature resolution of the focal plane arrays. Since the detection wavelength is only dependent on the size and on the materials forming the quantum well along with the barrier composition, a large spectral range can be covered with the same material by distinct QWIPs in the midinfrared. Specific functions like multicolor photodetection which is required for seeker and tracker systems can also be achieved on the same structure. Further advantages like radiation hardness represent also key features.

One of the main drawback of QWIPs is related to the background limited infrared performance (BLIP) temperature. This temperature T_{BLIP} corresponds to the temperature where the operation is limited by the background photon noise. The BLIP temperature is reached when the dark current is equal to the current generated by the background photons. Note that the BLIP temperature is estimated for a given field of view and a given background temperature. One of the parameters which governs the BLIP temperature is the capture probability of the photoexcited electrons. Under steady state operation, the capture probability is given by the ratio between the number of electrons captured in the well divided by the number of electrons flowing above the well. This capture probability is associated with the photoconductor gain which corresponds to the ratio between the number of carriers flowing through the external circuit divided by the number of mobile carriers generated in the active region. The typical time scale for the capture of the carriers in quantum wells is in the picosecond range. By comparison, for the competing low band-gap materials like HgCdTe generally used for infrared photodetection, the capture corresponds to an interband recombination process and occurs on a much longer time scale of the order of the microsecond. This difference explains that the BLIP temperature is higher for HgCdTe based materials than for GaAs QWIPs. HgCdTe detectors are at BLIP temperature at liquid-nitrogen temperature which is a key parameter for potential applications.

One has to keep in mind that the relevant properties for an infrared photodetector will depend on its specific targeted application, like the signal level to be measured (low or high flux conditions), the temperature of the background scene, the need for narrow or broadband photodetection, or the existence of a low-background as it is the case in space borne applications. The choice and the figure of merit of one material as compared to another is therefore not unequivocal. It is worth noting that photovoltaic detectors instead of photoconductive detectors have also been developed. These detectors are optimized when the capture probability become close to 1. However, their performances are lower than those related to photoconductive detectors.

Based on the experience acquired with QWIPs in the previous years, two key features to develop high-performance quantum dot infrared photodetectors are the following:

- to maintain a large absorption cross section for the intersublevel transitions;
- to decrease the capture probability of the carriers.

The polarization selection rule of the intersubband absorption, which is often cited in the literature as a key limitation for the operation or the development of QWIPs (only z-polarized transitions are optically active in the conduction band), is not a real limitation in terms of performance, since the use of grating couplers and the thinning of the substrate have proven to lead to highly efficient light coupling. In the case of quantum dots, normal incidence operation is allowed, thus avoiding the use of grating couplers which can be a drawback for counter measurements and targeting. However, the absorption cross section associated with the in-plane polarized transitions is often weak in the 3–5 μm and 8–12 μm spectral ranges as compared to the absorption cross section for optimized QWIPs, thus limiting the responsivity of the devices. The in-plane polarized intersublevel transitions with a large dipole matrix element (transitions between ground and first excited states) occur at long wavelengths ($\sim$20 μm) for standard InAs/GaAs quantum dots and are thus not suited for the infrared photodetection with a reasonable applied bias.

The relevant parameters to evaluate the photodetector performances have been the subject of numerous studies in the literature. Depending on the value of the capture probability and the number of active layers, a distinction is made between the noise gain and the photocurrent gain [65]. In the case of detectors with a small capture probability, the noise gain and the photocurrent gain are equivalent. It indicates that the discrete nature of the generation-recombination processes is not significant. Typical values of capture probability are around 0.1 in standard QWIPs. We restrict ourselves to this case in the following. The relevant parameters of the photodetector can be described as shown below. Following [66], noting p_c the capture probability of a carrier traversing a quantum dot layer, N the number of active periods, the photoconductive gain g is given by

$$g = 1/Np_c. \tag{8}$$

The generation-recombination noise current in QWIPs which results from the random thermal excitation of the carriers is given by

$$I_n^2 = 4eIg\Delta f(1 - p_c/2), \tag{9}$$

where e is the electronic charge, I the current flowing through the structure, and Δf the measurement bandwidth.

An important figure of merit of the detector is the detectivity D^* which is given by:

$$D^* = \frac{R\sqrt{A\Delta f}}{I_n}, \tag{10}$$

where $R = eg\eta/h\nu$ is the responsivity of the detector, and A is the detector surface. η corresponds to the product of the absorption quantum efficiency and the probability of the photoexcited carriers to escape from the quantum well.

Two situations can be considered. The first one corresponds to the case where the photodetector noise is dominated by the generation-recombination noise current. In this case, as the responsivity of the detector is proportional to the gain, the detectivity D^* is proportional to $1/(p_c(1 - p_c/2))^{1/2}$. We see that, if the current flowing through the detector is dominated by the dark current (i.e., nonbackground limited condition), the detectivity of the photoconductor can be maximized by minimizing the capture probability [67].

The second situation corresponds to the case where the photodetector noise is dominated by the fluctuation in the number of background photons. In this case, where the current is dominated by the photocurrent generated by the background flux photons (i.e., background limited operation), the detectivity becomes independent of the gain. Indeed, the detectivity can be written as $D^* \sim \eta g/(gI)^{0.5}$ with the current given by the relation $I = e\eta g\Phi_B$ where Φ_B is the background photon flux. We emphasize that the background limited detectivity exhibits a square root dependence on the absorption quantum efficiency. This latter parameter should therefore be maintained as high as possible. The dark current limited detectivity is linearly proportional to the absorption efficiency.

We note that the capture probability depends on the electric field which is not uniformly distributed in the structure and which varies in the presence or in the absence of infrared illumination [68]. Finally, it is important to emphasize that the transition between background limited or dark current limited operation depends on the capture probability. At a given temperature, the decrease of the capture probability can modify the operation of a detector from dark current limited operation to background limited operation. The decrease of the capture probability is expected to lead to an increase of T_{BLIP}.

Considering the infrared absorption properties of the intersublevel transitions in quantum dots, the realization of quantum dot infrared photodetectors (QDIP) has been proposed in the literature in the early 1990s [69]. Basically, the InAs/GaAs QDIPs can be expected to offer the same advantages as compared to the GaAs QWIPs in term of technology. Meanwhile, the slowing of the intradot relaxation process could provide an elegant way to decrease the capture probability and in turn to improve the infrared performances. Two-color photodetection might be achieved as it is the case for QWIPs. In the same time, the QDIPs are expected to benefit from all the technology developments made for the QWIPs, in particular for the specific readout circuitry. Two types of QDIPs have been proposed and investigated in the literature: (i) Vertical quantum dot infrared photodetectors; (ii) Lateral quantum dot infrared photodetectors. These structures are described below.

4.2. Vertical quantum dot infrared photodetectors

In a vertical quantum dot infrared photodetector, the photocurrent is collected through the vertical transport of carriers between top and bottom contacts. A typical electron QDIP structure is shown in Fig. 8. The conduction band profile of the device is shown in Fig. 9. The active region consists of 20 quantum dot layers separated by 35 nm thick GaAs barrier. The quantum dots are n-doped either in the dots or by modulation doping of the barriers. The doping density is adjusted in order to provide approximately 2 electrons per dot. The quantum dot layers are sandwiched between two n^+ GaAs doped layers. A 200 nm thick GaAs barrier separates the quantum dot multilayers from the contact layers. In order to measure the photocurrent, the samples are generally processed into square mesas (250×250 microns). The edge of the sample can be polished with 45° facets in order to test the polarization dependence of the photocurrent.

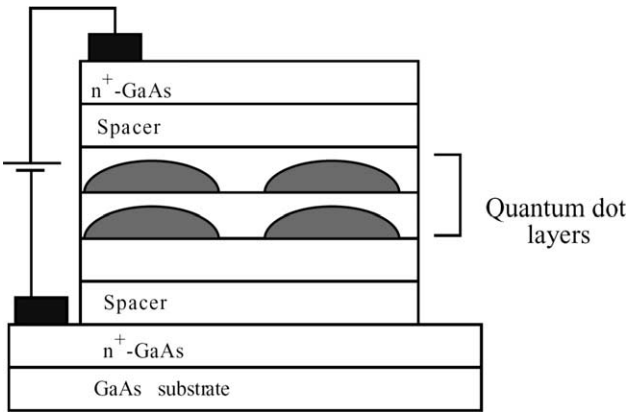

Fig. 8. Typical vertical quantum dot infrared photodetector structure. Only a fraction of the quantum dot layers is represented.

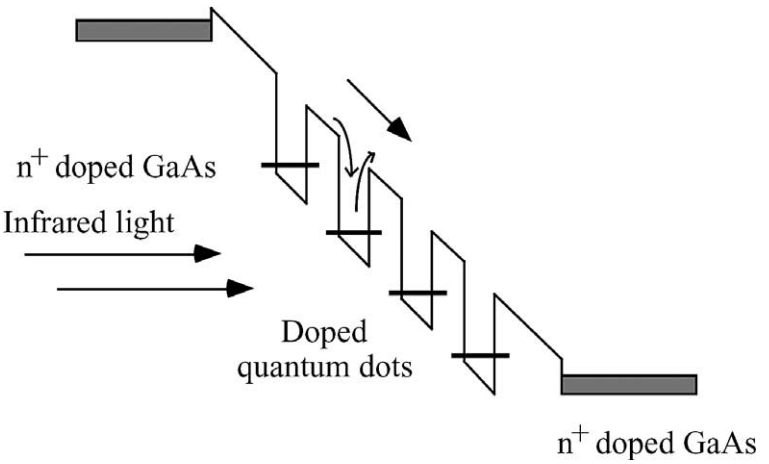

Fig. 9. Schematic conduction band profile of a quantum dot infrared photodetector structure.

We can observe that the simplest structure of an InAs/GaAs QDIP is very similar to that of a GaAs QWIP heterostructure. Some significant differences remain present: the discrete nature of the density of states that modifies the capture and the thermionic properties of the quantum dots – the nonuniformity of the quantum dot layers which modifies the carrier capture during the vertical transport. Obviously the modeling of the QDIP performances depends on the carrier relaxation time, the absorption cross section, the dark current and their dependences as a function of the applied bias. Improved performances as compared to QWIPs were predicted by Ryzhii et al. for dense arrays of small quantum dots [70]. However, the latter analysis did not account for the discrete energy spectrum of the dots and the carrier capture in the islands. Photoconductive gain and avalanche gain in InAs/GaAs quantum dot infrared photodetectors were calculated in [71] using Monte Carlo simulation. A photoconductive gain up to 10 was predicted for a bias voltage of 1 V. The carrier lifetime of QDIPs is however calculated with the same approximation used for quantum wells, i.e., not accounting for the specific relaxation mechanisms of the quantum dots.

A significant difference exists between standard GaAs/AlGaAs QWIPs and InAs/GaAs QDIPs. In the latter case, there is no blocking barrier, like the AlGaAs barrier, between the contact layers and the active region. This feature leads to a large dark current even at low applied bias. It has been shown that at low temperature the dark current in QDIPs is associated with a thermally activated tunneling from quantum dot levels into the wetting layer of the next period [72]. Experimentally, this increased dark current as compared to QWIPs explains partly the poor performances reported so far for quantum dot photodetectors. Several approaches can circumvent this problem. The growth of pseudomorphic InGaAs contact layers with a lower band gap could be considered. Alternatively, an AlGaAs blocking layer could be introduced in the vertical QDIP structure in order to limit the dark current [73]. One of the drawback of this approach is to shift the response to short wavelength and to decrease the responsivity. The introduction of an AlGaAs blocking layer covering the area between the quantum dots has also been proposed [74].

4.3. Lateral quantum dot photoconductor

It is interesting to note that both vertical or in-plane transport can be achieved with quantum dots. In-plane transport is not achievable with quantum wells since the contacts are shortened. This situation is not valid any more with quantum dots where the transport of the photoexcited carriers can occur laterally through the two-dimensional wetting layer [75] or a two-dimensional channel. The use of a two dimensional channel for the transport of the photoexcited carriers was first introduced by Lee and co-workers [76]. This approach takes advantage of the high mobility of the carriers in the 2D channel as well as the long lifetime of the photoexcited carriers. Fig. 12 shows a schematic description of this original structure. The carriers photoexcited resonantly through bound-to-continuum intersublevel transitions are transferred to the GaAs/AlGaAs heterointerface and drift laterally along this interface due to the applied electric field. The self-assembled quantum dots can be modulation doped by introducing a doping in the AlGaAs barrier or by using a standard doping of the islands. A strained InGaAs/GaAs quantum well can also be used as the high mobility lateral channel located close to the islands [77]. This structure can be viewed as a three-terminal device like a field-effect transistor. The high mobility and the long lifetime of the carriers lead to an improved responsivity. The lateral structure is also characterized by a lower dark current which is mainly associated with the interdot tunneling and hopping. The main drawback of these structures is the lower compatibility with the standard read-out circuitry and the difficulty to integrate them into focal plane arrays. Each pixel should require three terminals which remains challenging with the standard indium-bumped read-out circuitry.

4.4. Midinfrared photoconductivity

Fig. 10 shows a typical midinfrared photoconductivity spectrum of an InAs/GaAs vertical QDIP at low temperature (20 K) [33]. The wedge coupling geometry is shown in the inset. The *s* polarization corresponds to an electric field in the layer plane while the electric field of the *p*-polarized excitation has a component along the *z* growth axis and in the layer plane. The photocurrent exhibits an asymmetric line shape with a maximum around 225 meV and a large broadening (∼120 meV). The photocurrent is maximum for a *p*-polarized excitation but can also be observed for a *s*-polarized excitation. The photoresponse can be compared with the absorption spectrum measured on the same sample by using a multipass waveguide geometry (Fig. 11). The absorption in the midinfrared is similar to the one reported in Fig. 4. In this case, it is resonant around 160 meV. The absorption is dominated by a *z*-polarized transition between the ground state of the dots to the continuum. The absorption cross section for one quantum dot plane is around 2×10^{-14} cm^2, a value similar to those reported for QWIPs. The spectral shift between the absorption and the photocurrent resonance is associated with the escape of the carriers out of the dots following their photoexcitation. We note that the absorption is resonant for a transition between the ground state to the wetting layer states that lie at a lower energy as compared to the barrier continuum. The results reported in Fig. 10 indicate that the photoresponse of a QDIP can be easily measured for an in-plane polarized excitation, i.e., operation at normal incidence is feasible. It explains why many results in the literature have been reported on QDIP operating with an optical excitation at normal incidence, even if the oscillator strength of the in-plane polarized intersublevel transition is not maximum.

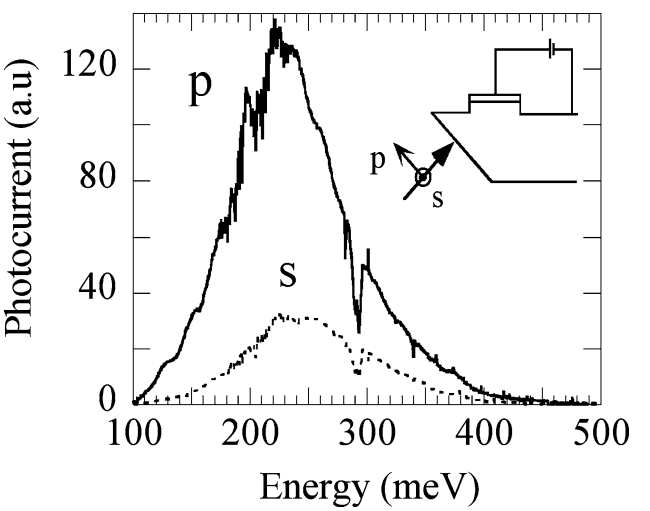

Fig. 10. Photoresponse of an InAs/GaAs quantum dot infrared photodetector at low temperature (20 K). The inset shows the wedge coupling geometry. The photoresponse is maximum for a *p*-polarized infrared excitation.

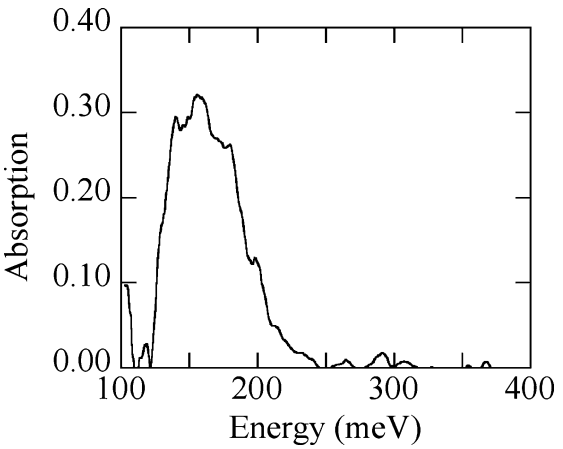

Fig. 11. Midinfrared absorption of the *n*-doped quantum dot sample measured in the multipass wave guide geometry. The absorption is deduced from the ratio of the transmission in *p* and *s* polarizations. This transmission ratio is normalized by the transmission ratio measured with a bulk GaAs substrate.

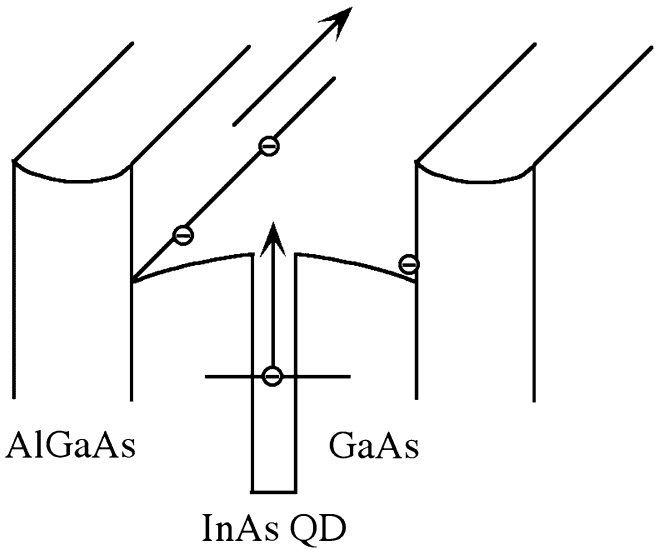

Fig. 12. Schematic conduction band profile of a lateral quantum dot infrared photodetector structure. The photoexcited carriers are transferred into the high mobility two-dimensional channel at the GaAs/AlGaAs heterointerface.

In the literature, the first observation of midinfrared photoconductivity with InAs quantum dots was reported in 1997 [78]. In the latter work, the authors did investigate InAs quantum dots separated by AlAs barriers. The quantum dot morphology was however not well-defined since one expects in this case a significant exchange between Al and In. The authors did use a Schottky contact to apply an electric field and their structure was therefore different from that of standard QDIPs. Far infrared photoconductivity in self-organized InAs quantum dots was reported in 1998 [79]. A standard *n*–*i*–*n* detector structure with *n*-doped GaAs barriers was investigated. A photoresponse with a resonance at 17 μm was observed for a normal-incidence infrared illumination. The photoresponse remained however very noisy due to the high temperature of the measurement (90 K) and could not be observed for a bias larger than 0.5 V. A detailed study of the photoresponse of InAs/GaAs quantum dot infrared photodetectors was reported by Maimon et al. [80]. The authors did measure the photoconductivity as a function of the polarization of the infrared excitation, i.e., not only at normal incidence. They have also performed the first measurement of the in-plane photoconductivity as opposed to vertical electronic transport in standard photoconductors. Though the authors could easily measure the photocurrent, they were not able to measure the midinfrared absorption of the samples. They have consequently concluded that the gain was much larger in QDIP than in QWIP since absorption and photocurrent are directly correlated in the latter case. However, no quantitative data were provided to support this assumption.

4.5. Performances of photodetectors

Few full characterizations of quantum dot photodetector devices have been reported so far. Most of the published work did focus on the study of the electronic structure of the dots through photocurrent spectroscopy. A short wavelength InGaAs photodetector with InGaP barriers was investigated by Kim et al. [81]. The photoconductivity was measured at normal incidence. At the peak wavelength of 5.5 μm, the responsivity was 130 mA/W and the detectivity was 4.74×10^7 cm · Hz$^{1/2}$/W at 77 K. This figure remains however lower by more than two orders of magnitude as compared to GaAs/AlGaAs QWIPs operating at the same wavelength. A normal incidence InGaAs quantum dot photodetector was also reported by Pan et al. [82]. In the latter case, the quantum dots had a low indium composition (30% nominal indium concentration). The onset of island growth occurs after the deposition of 9 monolayers instead of 1.8 monolayer in the case of the InAs/GaAs heterosystem. The performances of the devices were measured for a normal-incidence infrared illumination. A peak detectivity of 1×10^{10} cm · Hz$^{1/2}$/W was measured at 40 K and for a 13 μm peak wavelength. In view of the long wavelength operation of the device, this value remains surprisingly high. No quantitative comparison with the absorption amplitude was provided for this device. The same authors have recently reported on an InAs/GaAs QDIP peaked at 10 μm and operating at normal incidence [83]. A peak detectivity of 7×10^9 cm · Hz$^{1/2}$/W was achieved at 30 K. This value remains much weaker than the one achieved with state of the art quantum well infrared photodetectors.

Several groups have reported some results on QDIPs with AlGaAs barriers. Liu et al. have embedded 50 layers of InAs quantum dots in $Al_{0.33}Ga_{0.67}As$ barriers. The AlGaAs barriers induce a shift of the spectral response to high energy. At 80 K, a responsivity of 0.1 A/W at 5 μm was obtained for bias voltages ∼3 V [84]. Another approach consists in using an $Al_{0.3}Ga_{0.7}As$ current blocking barrier between the contacts and the active region. Detectivity values $D^* \sim 3 \times 10^9$ cm · Hz$^{1/2}$/W at 100 K were measured for a peaked photoresponse around 3.75 μm [85,86]. However the use of such AlGaAs blocking barrier suffers from one drawback: the barrier reduces the dark current and the photocurrent as well. Weak responsivities lower than 2 mA/W are thus obtained.

Most of the studies on QDIPs have dealt with *n*-doped quantum dots between two contact layers. A group has investigated photodetectors with undoped quantum dots. Their argument is that the dark current is higher in structures with a doped active region as compared to undoped active regions. In this case, one expects the photoresponse to exhibit a strong dependence as a function of the applied bias as well as a lower responsivity as compared to *n*-doped structures. Using AlGaAs blocking barriers, a detectivity $D^* \sim 10^{10}$ cm · Hz$^{1/2}$/W at 77 K with a photoresponse peaked at 6.2 μm and a −0.7 V bias was reported [87]. The responsivity was only 14 mA/W. Voltage controllable multiwavelength InAs quantum dot infrared photodetectors for mid and far infrared detection were also reported [88]. A bias controllable dual wavelength photoresponse (5.6 and 10 μm) could be achieved by incorporating two different quantum dot size distributions [89]. At 5.9 μm, peak detectivities $D^* = 5.8 \times 10^9$ cm · Hz$^{1/2}$/W at 77 K and 0.3 V applied bias were reported. The tailoring of the detection band of the photodetectors using InGaAs strain-relieving capping quantum wells was also demonstrated in these undoped structures [90].

The highest responsivities have been achieved using lateral quantum dot infrared photodetectors where the carrier transport is shifted to a neighboring channel with high electron mobility. Lee et al. have first reported a responsivity of 4.7 A/W at low temperature (10 K) for a 9 V applied bias [76]. More recently, Chu et al. have demonstrated a 11 A/W responsivity associated with a resonant photoresponse around 186 meV (6.65 μm) using an InGaAs channel layer [77]. The detector response time was 800 ms. The lateral quantum dot photodetectors exhibit very high responsivity values. However, the drawback is the lower compatibility of its architecture for focal plane arrays.

We emphasize that all the photoconductive detectors which have been reported so far involved transitions between the conduction states. Intraband photodetectors using valence states can also be envisaged. This applies in particular to the case of Ge/Si quantum dot devices where the band discontinuity is mostly located in the valence band. First observations of midinfrared photoconductivity in Ge/Si devices were reported recently [91,92].

4.6. Perspectives for improved performances

Despite their intrinsic potential advantages, the superiority of QDIPs over QWIPs has not yet been demonstrated. So far the reported detectivities are lower than those obtained with QWIPs. Lateral QDIPs have shown a strong potential to achieve high responsivities but their integration into focal plane arrays remains problematic. Several features can explain this situation. Most of the structures were investigated in a normal incidence geometry. This geometry provides a non vanishing photocurrent, but as we have shown, the bound-to-continuum absorption has only a weak absorption cross section for an in-plane polarization. The measured photoresponse at normal incidence is therefore not maximum. The intersublevel absorption between the ground and the first excited state (s–p transition) has a strong in-plane dipole matrix element. Unfortunately, this transition is resonant around 20 μm in standard InAs/GaAs quantum dots and does not give a photocurrent for a reasonable applied bias. In principle, one should reduce the lateral size of the quantum dots to tune the first *p*-excited state close to the continuum while keeping a large quantum dot density. In this situation, the major in-plane intersublevel oscillator strength would be concentrated on

the bound-to-continuum transition, an ideal situation to obtain a high in-plane polarized responsivity. Such structures have not been demonstrated so far. We note that an improvement in the quantum dot uniformity would decrease the inhomogeneous broadening of the intersublevel transitions and increase the responsivity of the devices. It is obvious that the standard QDIPs on GaAs suffer from a large dark current as no blocking barriers are present between the injectors and the active region. The introduction of AlGaAs barriers reduce the dark current and the photocurrent as well. A solution that has not been yet studied is the design of strained InGaAs injector layers with a lower band gap as compared to GaAs. This type of layers has not been demonstrated to date. Finally, one of the potential advantage of QDIPs was associated with a longer relaxation time as compared to quantum wells. While this relaxation time can be large as shown by the measurements on the polaron relaxation, it does exhibit a strong dependence as a function of the carrier density. Auger-assisted mechanisms are very efficient at high injected carrier densities. It is likely that the relaxation time is not as large as expected under the standard operation conditions of the QDIPs. Further work is needed to clarify the dependence of the capture time of the carriers as a function of the applied bias.

5. Conclusion

We have presented a review on the midinfrared properties of InAs/GaAs semiconductor self-assembled quantum dots. The electronic structure of the islands was obtained by solving the 3D Schrödinger equation in a 8-band **k**.**p** formalism. The strain field in the islands was calculated using a valence force field method. The *n*-doped InAs/GaAs quantum dots exhibit bound-to-bound and bound-to-continuum intersublevel absorption in the midinfrared. We have shown that the electron-phonon interaction is modified in quantum dots and corresponds to a strong coupling regime. This leads to the formation of mixed electron-phonon quasiparticles (polarons). The relaxation dynamic of the polaron depends on the weight of the 1-phonon component in the wave function. The principle of operation of vertical and lateral quantum dot infrared photodetectors has been described and compared to the one of infrared photodetectors. The performances of several types of detectors were discussed. It appears that the performances reported to date for vertical quantum dot infrared photodetectors are inferior to those reported for QWIPs. The origin of this situation has been discussed and new directions to develop high performance quantum dot infrared photodetectors have been proposed.

Acknowledgements

It is a pleasure to thank Jean-Michel Gérard, Véronique Thierry-Mieg and Aristide Lemaître for the growth of the InAs/GaAs quantum dot samples along with numerous fruitful discussions. We thank G. Fishman for numerous scientific discussions. We are also grateful to Jean-Michel Ortega for his assistance in the free-electron laser experiments and his constant support. Collaboration with Professor E. Finkman is acknowledged.

References

[1] L.C. West, S.J. Eglash, Appl. Phys. Lett. 46 (1986) 1156.
[2] B.F. Levine, J. Appl. Phys. 74 (1993) R1.
[3] U. Bockelmann, G. Bastard, Phys. Rev. B 42 (1990) 8947.
[4] S. Tarucha, D.G. Austing, T. Honda, R.J. Van der Hage, L.P. Kouwenhoven, Phys. Rev. Lett. 77 (1997) 3613.
[5] R.H. Blick, R.J. Haug, J. Weis, D. Pfannkuche, K.V. Klitzing, K. Eberl, Phys. Rev. B 53 (1996) 7899.
[6] Ch. Sikorski, U. Merkt, Phys. Rev. Lett. 62 (1989) 2164.
[7] T. Demel, D. Heitmann, P. Grambow, K. Ploog, Phys. Rev. Lett. 64 (1990) 788.
[8] I.N. Stranski, L. Krastanow, Sitzungsber. Akad. Wiss. Wien Math. Naturwiss. K1 Abt. 2B Chemie 146 (1937) 797.
[9] L. Goldstein, F. Glas, J.Y. Marzin, M.N. Charasse, G. Le Roux, Appl. Phys. Lett. 47 (1985) 1099.
[10] Y.W. Mo, D.E. Savage, B.S. Swartzentruber, M.G. Lagally, Phys. Rev. Lett. 65 (1990) 1020.
[11] J.M. Gérard, J.Y. Marzin, G. Zimmermann, A. Ponchet, O. Cabrol, D. Barrier, B. Jusserand, B. Sermage, Solid State Electron. 40 (1996) 807.
[12] M. Grundmann, O. Stier, D. Bimberg, Phys. Rev. B 52 (1995) 11969.
[13] H. Lee, R. Lowe-Webb, W. Yang, P.C. Sercel, Appl. Phys. Lett. 72 (1998) 812.
[14] J.-Y. Marzin, G. Bastard, Solid State Commun. 92 (1994) 437.
[15] Ph. Lelong, G. Bastard, Solid State Commun. 98 (1996) 819.
[16] L.R.C. Fonseca, J.L. Jimenez, J.P. Leburton, R.M. Martin, Phys. Rev. B 57 (1998) 4017.
[17] A. Wojs, P. Hawrylak, S. Fafard, L. Jacak, Phys. Rev. B 54 (1996) 5604.
[18] S. Sauvage, P. Boucaud, J.-M. Gérard, V. Thierry-Mieg, Phys. Rev. B 58 (1998) 10562.

[19] M.A. Cusack, P.R. Briddon, M. Jaros, Phys. Rev. B 54 (1996) R2300.
[20] M.A. Cusack, P.R. Briddon, M. Jaros, Phys. Rev. B 56 (1997) 4047.
[21] H. Jiang, J. Singh, Appl. Phys. Lett. 71 (1997) 3239.
[22] H. Jiang, J. Singh, Phys. Rev. B 56 (1997) 4696.
[23] C. Pryor, Phys. Rev. B 57 (1998) 7190.
[24] W. Sheng, J.-P. Leburton, Appl. Phys. Lett. 78 (2002) 1258.
[25] O. Stier, M. Grundmann, D. Bimberg, Phys. Rev. B 59 (8) (1999) 5688.
[26] F. Bras, P. Boucaud, S. Sauvage, G. Fishman, J.-M. Gérard, Appl. Phys. Lett. 80 (2002) 4620.
[27] S. Sauvage, P. Boucaud, R.P.S.M. Lobo, F. Bras, G. Fishman, R. Prazeres, F. Glotin, J.-M. Ortéga, J.-M. Gérard, Phys. Rev. Lett. 88 (2002) 177402.
[28] J. Kim, L.-W. Wang, A. Zunger, Phys. Rev. B 57 (1998) R9408.
[29] S. Sauvage, P. Boucaud, T. Brunhes, A. Lemaître, J.-M. Gérard, Phys. Status Solidi B 224 (2001) 579.
[30] H. Drexler, D. Leonard, W. Hansen, J.P. Kotthaus, P.M. Petroff, Phys. Rev. Lett. 73 (1994) 2252.
[31] S. Sauvage, P. Boucaud, J.-M. Gérard, V. Thierry-Mieg, J. Appl. Phys. 84 (1998) 4356.
[32] S. Sauvage, P. Boucaud, T. Brunhes, A. Lemaître, J.M. Gérard, Phys. Rev. B 60 (1999) 15589.
[33] S. Sauvage, P. Boucaud, T. Brunhes, V. Immer, E. Finkman, J.-M. Gérard, Appl. Phys. Lett. 78 (2001) 2327.
[34] S. Sauvage, P. Boucaud, F. Glotin, R. Prazeres, J.-M. Ortega, A. Lemaître, J.-M. Gérard, V. Thierry-Mieg, Phys. Rev. B 59 (1999) 9830.
[35] T. Brunhes, P. Boucaud, S. Sauvage, F. Glotin, R. Prazeres, J.-M. Ortega, A. Lemaître, J.-M. Gérard, Appl. Phys. Lett. 75 (1999) 835.
[36] T. Brunhes, P. Boucaud, S. Sauvage, A. Lemaître, J.-M. Gérard, F. Glotin, R. Prazeres, J.-M. Ortega, Phys. Rev. B 61 (2000) 5562.
[37] S. Sauvage, T. Brunhes, P. Boucaud, A. Lemaître, J.-M. Gérard, F. Glotin, R. Prazeres, J.-M. Ortega, Phys. Status Solidi B 224 (2001) 595.
[38] S. Sauvage, P. Boucaud, T. Brunhes, F. Glotin, R. Prazeres, J.-M. Ortega, J.-M. Gérard, Phys. Rev. B 63 (2001) 113312.
[39] D. Leonard, M. Krishnamurthy, C.M. Reaves, S.P. Denbaars, P.M. Petroff, Appl. Phys. Lett. 63 (1993) 3203.
[40] M. Grundmann, N.N. Ledentsov, R. Heitz, L. Eckey, J. Christen, J. Böhrer, D. Bimberg, S.S. Ruvimov, P. Werner, U. Richter, J. Heydenreich, V.M. Ustinov, A.Yu. Egorov, A.E. Zhukov, P.S. Kopev, Zh.I. Alferov, Phys. Status Solidi 188 (1995) 249.
[41] Y. Hasegawa, H. Kiyama, Q.K. Xue, T. Sakurai, Appl. Phys. Lett. 72 (1998) 2265.
[42] B. Legrand, B. Grandidier, J.P. Nys, D. Stiévenard, J.M. Gérard, V. Thierry-Mieg, Appl. Phys. Lett. 73 (1998) 96.
[43] P.N. Keating, Phys. Rev. 145 (1966) 637.
[44] G. Fishman, Energie et fonction d'onde des semi-conducteurs, Les editions de physique, 1988.
[45] G. Bastard, Wave Mechanics Applied to Semiconductor Heterostructures, Les editions de physique, 1992.
[46] G.L.G. Sleijpen, H.A. van der Vorst, SIAM J. Matrix Anal. Appl. 17 (1996) 401.
[47] H.C. Liu, M. Buchanan, Z.R. Wasilewski, Appl. Phys. Lett. 72 (1998) 1682.
[48] S. Sauvage, Propriétés infrarouges des boîtes quantiques semi-conductrices InAs/GaAs, Thèse de l'université Paris-XI, Mars 1999.
[49] H. Benisty, C.M. Sottomayor-Torrès, C. Weisbuch, Phys. Rev. B 44 (1991) 10945.
[50] T. Inoshita, H. Sakaki, Phys. Rev. B 46 (1992) 7260.
[51] U. Bockelmann, T. Egeler, Phys. Rev. B 46 (1992) 15574.
[52] T. Inoshita, H. Sakaki, Phys. Rev. B 56 (1997) R4355.
[53] O. Verzelen, R. Ferreira, G. Bastard, Phys. Rev. B 62 (2000) R4809.
[54] S. Hameau, J.N. Isaia, Y. Guldner, E. Deleporte, O. Verzelen, R. Ferreira, G. Bastard, J. Zeman, J.M. Gérard, Phys. Rev. Lett. 83 (1999) 4152.
[55] D. Von der Linde, J. Khul, H. Klingerberg, Phys. Rev. Lett. 44 (1980) 1505.
[56] X.-Q. Li, Y. Arakawa, Phys. Rev. B 57 (12) (1998) 285.
[57] X.-Q. Li, H. Nakayama, Y. Arakawa, Phys. Rev. B 59 (1999) 5069.
[58] Ph. Lelong, S.H. Lin, Appl. Phys. Lett. 81 (2002) 1002.
[59] S. Sauvage, P. Boucaud, F. Glotin, R. Prazeres, J.-M. Ortega, A. Lemaître, J.-M. Gérard, V. Thierry-Mieg, Appl. Phys. Lett. 73 (1998) 3818.
[60] S. Hadachi (Ed.), Properties of Aluminium Gallium Arsenide, INSPEC, London, 1993.
[61] O. Verzelen, R. Ferreira, G. Bastard, Phys. Rev. B 64 (2001) 075315.
[62] O. Verzelen, R. Ferreira, G. Bastard, Phys. Rev. Lett. 88 (2002) 146803.
[63] O. Verzelen, G. Bastard, R. Ferreira, Phys. Rev. B 66 (2002) 081308(R).
[64] F. Vallée, F. Bogani, Phys. Rev. B 43 (1991) 12049.
[65] M. Ershov, H.C. Liu, J. Appl. Phys. 86 (1999) 6580.
[66] W.A. Beck, Appl. Phys. Lett. 63 (1993) 3589.
[67] B.F. Levine, Appl. Phys. Lett. 74 (1999) 892.
[68] L. Thibaudeau, P. Bois, J.Y. Duboz, J. Appl. Phys. 79 (1996) 446.
[69] C. Weisbuch, B. Vinter, Quantum Semiconductor Structures, Academic Press, 1991.
[70] V. Ryzhii, I. Khmyrova, V. Mitin, M. Stroscio, M. Willander, Appl. Phys. Lett. 78 (2001) 3523.
[71] B. Kochman, A.D. Stiff-Roberts, S. Chakrabarti, J.D. Phillips, S. Krisna, J. Singh, P. Bhattacharya, IEEE J. Quantum Electron. 39 (2003) 459.
[72] J.-Y. Duboz, H.C. Liu, Z.R. Wasilewski, M. Byloss, R. Dudek, J. Appl. Phys. 93 (2003) 1320.
[73] A.D. Stiff, S. Krishna, P. Bhattacharya, S. Kennerly, Appl. Phys. Lett. 79 (2001) 421.
[74] V. Ryzhii, J. Appl. Phys. 89 (2001) 5117.
[75] L. Chu, A. Zrenner, G. Böhm, G. Abstreiter, Appl. Phys. Lett. 76 (2000) 1944.

[76] S.-W. Lee, K. Hirakawa, Y. Shimada, Appl. Phys. Lett. 75 (1999) 1428.
[77] L. Chu, A. Zrenner, M. Bichler, G. Abstreiter, Appl. Phys. Lett. 79 (2001) 2249.
[78] K.W. Berryman, S.A. Lyon, M. Segev, Appl. Phys. Lett. 70 (1997) 1861.
[79] J. Phillips, K. Kamath, P. Bhattacharrya, Appl. Phys. Lett. 72 (1998) 2020.
[80] S. Maimon, E. Finkman, G. Bahir, S.E. Schacham, J.M. Garcia, P.M. Petroff, Appl. Phys. Lett. 73 (1998) 2003.
[81] S. Kim, H. Mohseni, M. Erdtmann, E. Michel, C. Jelen, M. Razeghi, Appl. Phys. Lett. 73 (1998) 963.
[82] D. Pan, E. Towe, S. Kennerly, Appl. Phys. Lett. 73 (1998) 1937.
[83] D. Pan, E. Towe, S. Kennerly, Appl. Phys. Lett. 75 (1999) 2719.
[84] H.C. Liu, M. Gao, J. McCaffrey, Z.R. Wasilewski, S. Fafard, Appl. Phys. Lett. 78 (2001) 79.
[85] A.D. Stiff, S. Krishna, P. Bhattacharya, S.W. Kennerly, IEEE J. Quantum Electron. 37 (2001) 1412.
[86] A.D. Stiff, S. Krishna, P. Bhattacharya, S. Kennerly, Appl. Phys. Lett. 79 (2001) 421.
[87] Z. Ye, J.C. Campbell, Z. Chen, E. Kim, A. Madhukar, IEEE J. Quantum Electron. 38 (2002) 1234.
[88] Z. Ye, J.C. Campbell, Z. Chen, E. Kim, A. Madhukar, J. Appl. Phys. 92 (2002) 4141.
[89] Z. Chen, E. Kim, A. Madhukar, Appl. Phys. Lett. 80 (2002) 2490.
[90] E.T. Kim, Z. Chen, A. Madhukar, Appl. Phys. Lett. 79 (2001) 3341.
[91] L.P. Rokhinson, D.C. Tsui, J.L. Benton, Y.-H. Xie, Appl. Phys. Lett. 75 (1999) 2413.
[92] N. Rappaport, E. Finkman, T. Brunhes, P. Boucaud, S. Sauvage, N. Yam, V. Le Thanh, D. Bouchier, Appl. Phys. Lett. 77 (2000) 3224.